Astronomy & Astrophysics

LETTER TO THE EDITOR

Polarization echoes from past nuclear activity in the quasi-periodic eruption source GSN 069

B. Agís-González[1,2,3,★] , D. Hutsemékers[3] , I. Liodakis[1] , S. Cazzoli[2] , D. Sluse[3] , G. Miniutti[4] , I. Márquez[2] ,
J. Masegosa[2] , F. Marin[5] , J. A. Acosta-Pulido[6,7], and C. Ramos Almeida[6,7]

[1] Institute of Astrophysics, FORTH, N.Plastira 100, Vassilika Vouton 70013 Heraklion, Greece
[2] Instituto de Astrofísica de Andalucía, IAA-CSIC, Glorieta de la Astronomía, s/n, 18008 Granada, Spain
[3] Institut d'Astrophysique et de Géophysique, Université de Liège, Allée du 6 Août 19c, 4000 Liège, Belgium
[4] Centro de Astrobiología (CAB), CSIC-INTA, Camino Bajo del Castillo s/n, 28692, Villanueva de la Cañada Madrid, Spain
[5] Université de Strasbourg, CNRS, Observatoire Astronomique de Strasbourg, UMR 7550, F-67000 Strasbourg, France
[6] Instituto de Astrofísica de Canarias, Calle Vía Láctea, s/n, E-38205 La Laguna, Tenerife, Spain
[7] Departamento de Astrofísica, Universidad de La Laguna, E-38206 La Laguna, Tenerife, Spain

Received 20 September 2025 / Accepted 9 December 2025

ABSTRACT

Context. X-ray quasi-periodic eruptions (QPEs) are repeating, high-amplitude, soft X-ray bursts observed from the nuclei of a dozen nearby low-mass galaxies. Their origin remains a major puzzle in the physics of accretion variability. Observational data indicate that X-ray and/or optical tidal disruption events (TDEs) may precede QPE detections. Although both kinds of outburst are driven by supermassive black holes, they are more frequently detected in faded active galactic nuclei (AGNs), when the TDE is not happening in a dormant galaxy. In the case of the QPE discovery source, GSN 069, observations and simulations have revealed evidence of past nuclear activity, although it remains debated whether this activity arose from a past AGN phase or from an enhanced TDE rate.
Aims. We investigated the origin of the past nuclear activity in GSN 069.
Methods. Past AGN activity imprints detectable polarization in optical light, due to the expected delay between direct and scattered light. On 6 September 2019, we targeted GSN 069 with VLT/FORS2 in both imaging polarimetry and spectropolarimetry modes so that its optical polarization could be investigated while the first detected QPE phase was still active.
Results. We measured a rising polarization, from ∼0% to ∼1.5%, as moving away from the nucleus of GSN 069. This rise is probed to be intrinsic to the central engine, confirming the already detected extended emission line region (EELR) by integral field unit data.
Conclusions. The increasing radial polarization demonstrates a switched-off nucleus. The polarization angle traces an axis aligned with elongated [OIII], [NII], and Hα gas distributions, revealing an EELR that may be consistent with relic polarization cones, therefore suggesting the presence of a torus-like structure in the past. Thus, optical polarization echoes geometrically favor a faded AGN as the origin of the EELR rather than a past elevated TDE rate, although the latter cannot be excluded.

Key words. techniques: polarimetric – galaxies: active – galaxies: nuclei – galaxies: Seyfert

1. Introduction

Systematic multi-wavelength sky surveys have opened a new era in detecting nuclear transients (NTs), i.e., outbursts in galactic nuclei driven by accretion variability onto supermassive black holes. The recently discovered quasi-periodic eruptions (QPEs, Miniutti et al. 2019) are striking, high-amplitude (several orders of magnitude), quasi-periodic X-ray bursts of variable duration (1–100 hours), recurring on timescales of hours to weeks. Their origin remains a mystery, though 12 sources have now been confirmed (Miniutti et al. 2019; Giustini et al. 2020; Arcodia et al. 2021; Chakraborty et al. 2021; Quintin et al. 2023; Arcodia et al. 2024; Nicholl et al. 2024; Hernández-García et al. 2025; Bykov et al. 2025; Chakraborty et al. 2025; Arcodia et al. 2025). Some showed either X-ray (GSN069, Miniutti et al. 2023; XMMSL1 J024916.6-041244J0249 Chakraborty et al. 2021) or optical (AT2019qiz, Nicholl et al. 2024; AT2019vcb, Bykov et al. 2025; AT2022upj, Chakraborty et al. 2025) tidal disruption events

(TDEs) prior to the QPE detection. This TDE–QPE link has motivated the TDE+EMRI=QPEs model (Linial & Metzger 2023; Linial et al. 2025), where a stellar object, brought into the nucleus as an extreme mass-ratio inspiral (EMRI), passes twice per orbit through an existing accretion disk on a low-eccentricity orbit, reproducing the observed properties of QPE flares. In addition, TDE and QPE hosts also show a preference for extended emission line regions (EELRs) (French et al. 2023; Wevers & French 2024; Wevers et al. 2024).

GSN 069, like the other QPE sources, is X-ray unobscured (Miniutti et al. 2013), while its current X-ray emission is compatible with a compact TDE-like accretion disk (Guolo et al. 2025) that switched on at least 8 years before the first QPE detection in December 2018. However, no optical broad emission lines (BELs) were detectable in deep long-slit (Wevers et al. 2022) or in MUSE integral field unit data (Wevers et al. 2024). The MUSE data revealed a ∼10kpc EELR, photoionized by a nonstellar continuum exceeding two to three times the current nuclear luminosity, pointing to nuclear activity that shut down thousands of years ago (Wevers et al. 2024). This past energy

budget could be accomplished by two different scenarios: either a faded AGN (French et al. 2023; Wevers et al. 2024) or a past elevated TDE rate as photoionizing engine (Mummery et al. 2025). In both cases, considering that the recent TDE-like activity is unable to sustain mature BELs, only narrow-emission lines (NELs) and the EELR remain observable as fossil records of the past nuclear activity. Hutsemékers et al. (2019) have proposed that a past bright AGN phase imprints an echo in polar-scattered light, thus producing detectable polarization. For this Letter we tested this scenario for GSN069 by resolving the distribution of the polarized flux until ~2kpc from the nucleus with VLT/FORS2 photo- and spectropolarimetry data taken on 6 September 2019, when the first detected QPE phase of GSN069 was still active, after the decay of a TDE-like X-ray flare first detected in 2010 and preceding a second X-ray rebrightening possibly associated with a repeated TDE (Miniutti et al. 2023).

2. Direct spectrum and polarization of GSN069

Details of the observations and data analysis are provided in Appendix A. We found a bright feature located 4.25″ south of the nucleus (hereafter the southern spot) in our FORS2 PMOS spectral images (Fig. B.1). The southern spot is also present in X-ray Chandra data (Extended Data Fig. 1 in Miniutti et al. 2019) and in the MUSE continuum-subtracted Hα image (Fig. B.2), although it is not resolved in our FORS2 IPOL optical images (Fig. 1). Therefore, in addition to the direct spectrum and polarization of the nucleus, we also analyzed the spectra extracted from the southern spot and from two regions in the host galaxy, ~1.75″ north and south of the nucleus (see Fig. 1 and Appendices A.3 and C). At the distance of GSN 069 ($z = 0.0181$; Miniutti et al. 2013), $1'' \simeq 380$ pc.

2.1. Direct spectrum

Figure A.1 shows the optical direct spectra of the GSN 069 nucleus and the southern spot, while Fig. C.1 presents the north and south extractions. After subtracting the computed starlight model, no continuum emission remains or broad Balmer line components arise in any extraction (see Appendices A.3, D). Nonetheless, the standard emission-line ratios used in BPT diagnostics (e.g., Kewley et al. 2001) classify GSN 069 as an AGN at the nucleus, southern spot, and both host-galaxy regions. Combined with the absence of X-ray obscuration, this indicates that the current nuclear activity has shut down and it is unable to sustain a persistent broad-line region. We are therefore observing a relic narrow-line region compatible with either a faded AGN phase (Wevers et al. 2024) or a past enhanced rate of TDEs (Mummery et al. 2025).

2.2. Imaging polarimetry

With our IPOL data, we found a good compromise between capturing the full nuclear emission and minimizing host-galaxy contamination by choosing an aperture radius of approximately three times the value of the seeing, i.e., ~3σ; σ remained stable at around 0.7″ during the observations. This yielded a polarization degree of $p = 0.15 \pm 0.11\%$ and a polarization position angle of $\theta = 126° \pm 20°$. Following Plaszczynski et al. 2014, the debiased polarization degree is $p_0 = 0.12 \pm 0.11\%$, certainly compatible with null polarization. However, as we increased the aperture radius, p also increased and θ became better defined (see Table 1). Figure 1 shows the different integration circular apertures with radii 3σ (2.1″), 5σ (3.5″), 7σ (4.9″), and 9σ (6.3″) on the acquisition image of GSN 069. The radial trend
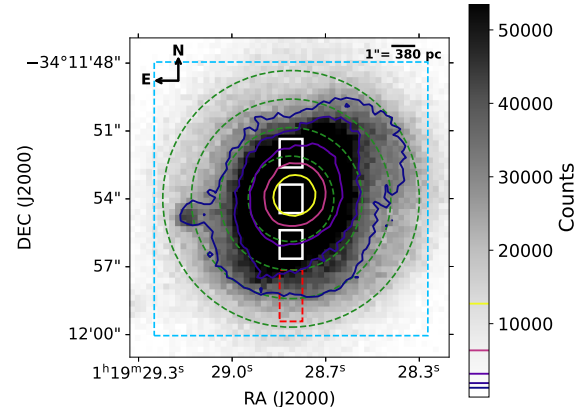
Fig. 1. Acquisition image of GSN 069. Flux contours follow the shown color scale. The green dashed circles mark IPOL aperture areas with radii of ~3σ (2.1″), ~5σ (3.5″), ~7σ (4.9″), and ~9σ (6.3″), where σ is the seeing value during IPOL observations, which remained stable at ~0.7″. The white boxes indicate the north, nucleus, and south regions used for PMOS extractions (see text), while the red box show the southern spot extraction region. The blue dashed box outlines the same 12″×12″ area as the Chandra image of GSN 069 shown in panel d of Extended Data Fig. 1 in Miniutti et al. 2019. The spot is not visible in our optical FORS2 IPOL images, but appears in those Chandra observations and in the MUSE continuum-subtracted Hα image (Fig. B.2 and Appendix B).

Table 1. Imaging polarimetry results for different aperture radii, r_{aper}, in seeing units, where $\sigma = 0.7''$. p_0 is the debiased polarization degree.

r_{aper} (σ)	q (%)	u (%)	p (%)	p_0 (%)	θ (°)
3	−0.05	−0.15	0.15 ± 0.11	0.12	126 ± 20
5	−0.08	−0.34	0.35 ± 0.10	0.34	129 ± 8
7	−0.00	−0.54	0.54 ± 0.10	0.53	135 ± 5
9	0.11	−0.76	0.77 ± 0.10	0.76	139 ± 4

is evident in Fig. 2, where p is measured in annular apertures (represented in Fig. B.2) instead of circular apertures to exclude the nucleus, revealing a net rotation of θ with distance. The radio emission of GSN 069, consistent with a compact outflow associated with the ongoing X-ray TDE activity (Goodwin et al. 2025), prevents an estimation of its symmetry axis, and thus a comparison with θ is not feasible. Figure 1 in Guolo et al. (2025), which decomposes the radial profile using HST F606W images (similar wavelength coverage to our data; see Appendix A.1), suggests that our smallest aperture, 2.1″, isolates the switched-off nucleus, while larger apertures encompass the EELR/ionization cones. This scenario is further analyzed in the following sections.

Unpolarized starlight from the host galaxy could dilute the intrinsic nuclear polarization, as it is coupled to the nuclear flux emission (e.g., Miller & Antonucci 1983; Marin 2018). We tried to estimate the host contribution at each aperture radius by using our IPOL acquisition image (60 s integration, no stripped mask used). We modeled GSN 069 as the sum of (1) a 2D Gaussian with the FWHM fixed to the seeing value, representing the nucleus as a point source, and (2) a convolved Sersic profile (Sérsic 1968) with n=4, i.e., deVaucouleurs law (de Vaucouleurs 1948) representing the host galaxy. This general model suggests that the host intensity exceeds the nuclear contribution by a factor of ~10 at our smaller aperture radius, i.e., 2.1″, consistent
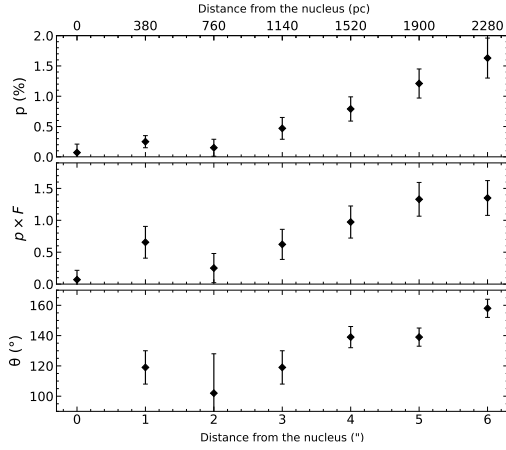
Fig. 2. Polarization degree (p), polarized flux ($p \times F$ in arbitrary units), and polarization angle (θ) measured in the V band, through an aperture of 4 pixels of diameter (1″) centered on the nucleus, and in 4 pixel wide annuli of increasing radius (1″ ≃ 380 pc). The polarization degree is not corrected for the bias. The first bin is circular (nucleus) showing p compatible with zero and an undefined θ.
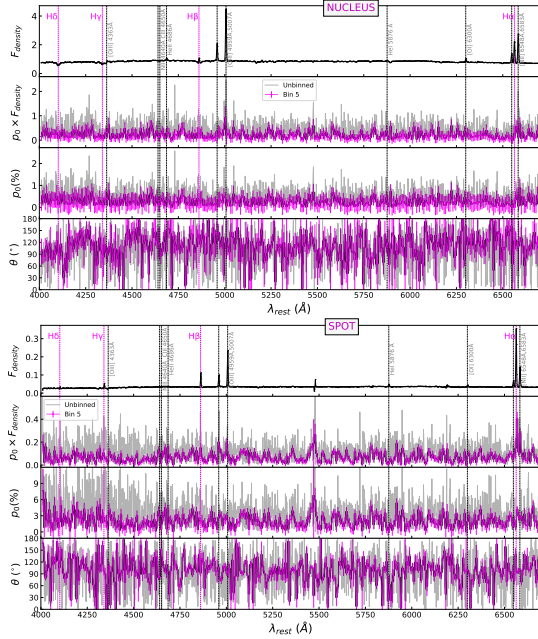

Fig. 4. Polarization degree and angle measured in spatial bins (subslits) along the slit. The polarization degree is not corrected for the bias. The bin centered on the nucleus is 5 spatial pixels (1.25″) long. The subsequent bins are 3, 3, 5, 6, and 7 pixels long. Positive distances are toward the north, negative ones toward the south (1″ ≃ 380 pc). Measurements integrated over the continuum wavelength ranges 3800–5000 Å< and 5400–6600 Å are shown in blue and red, respectively. The bin at −4.1″ contains the southern spot.

Fig. 3. Flux density in arbitrary units (F_{density}), debiased polarization degree (p_0), polarized flux ($F_{\text{density}} \times p_0$), and polarization angle (θ) for the nucleus (upper panel) and southern spot (lower panel).

with the radial decomposition by Guolo et al. (2025). The low spatial resolution of our acquisition image, together with the coupling of the nuclear intrinsic emission with the host contribution, prevents meaningful constraints on a proper host correction. Nevertheless, the observed increasing polarization with radius implies that, despite gathering more and more host galaxy inside the aperture, there is no depolarizing effect, even at the location of the star-forming ring revealed by MUSE data (Wevers et al. 2024) at radius ∼2″.

2.3. Spectropolarimetry

Figure 3 shows the direct spectrum, the polarized spectrum, the debiased polarization degree, and the polarization position angle
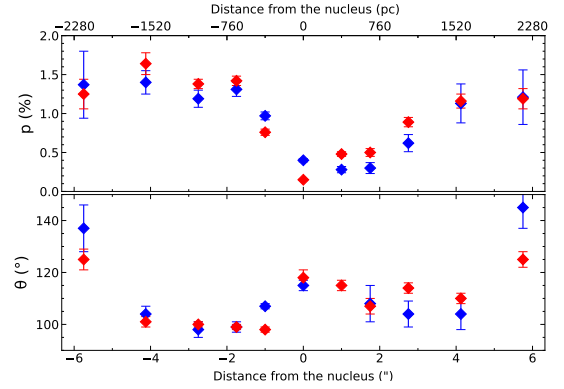
for the nucleus and the southern spot. Figure C.2 shows the same data for the two regions north and south of the nucleus. In general, and particularly in the nucleus, the polarization signal is low, yielding a low signal-to-noise ratio (S/N). The noise hampers accurate line identification in the polarized spectra, and $\theta(\lambda)$ remains poorly define due to the low polarization degree.

We averaged the Stokes parameters q and u between 5100 and 6500 Å (line-free range) to compute the corresponding continuum polarization degree $p_{5100–6500}$ (not debiased to compare with Fig. 2 and Fig. 4) and polarization angle $\theta_{5100–6500}$, assigning σ_p as the 1σ error and adopting $\sigma_\theta = 28.65° \frac{\sigma_p}{p}$ (Bagnulo et al. 2009). We obtained respectively $p_{5100–6500} = 0.22\% \pm 0.02\%$ and $\theta_{5100–6500} = 111° \pm 2°$ for the nucleus, $0.35\% \pm 0.04\%$ and $105.00° \pm 3°$ for the north, $1.20\% \pm 0.05\%$ and $102° \pm 1°$ for the south, and $1.5\% \pm 0.11\%$ and $98° \pm 2°$ for the southern spot. In agreement with imaging polarimetry, polarization increases as we move away from the nucleus. Figure 4 shows the polarization measured in spatial bins (see Fig. B.2 for their exact location). That binning reveals an asymmetry: p is higher in the south than in the north, with the southern spot (contained in the −4.1″ bin) matching the south region within the errors. θ rotates between the north and south and the southern spot regions. The bins at ±6″ deviate from this trend with $\theta \sim 140°$ in both north and south. As seen in Fig. B.2, these bins lie near the edge of the EELR, where a change in the dominant polarization mechanism may occur.

As in the imaging polarimetry analysis (Sect. 2.2), we attempted to estimate the contribution of the host galaxy to the spectropolarimetric measurements. We modeled the stellar continuum and absorption features, as done for the direct spectra, for each ordinary and extraordinary beam. Since the nuclear continuum is almost completely removed after starlight subtraction, residual noise or slight mismatches in the scaling of the stellar model introduce spurious flux values, yielding artificially high $p(\lambda)$ and meaningless $\theta(\lambda)$. Fortunately, the polarized flux, $p \times F$, should remain unaffected by starlight dilution (Tran 1995), provided the starlight is entirely unpolarized.

We also searched for broad Balmer emission lines in the polarized flux via line-profile fitting (see Appendix D). Although the S/N is not optimal, no broad components are detected in the nucleus, the spot, or the two other regions. In contrast, the

brightest narrow emission lines ([OIII], Hα+[NII]) are seen in the polarized flux, especially in the southern regions.

3. Discussion

Both photo- and spectropolarimetry show that the polarization of GSN 069 is null or very small at the nucleus, but gradually increases up to 1.5% at distances of about 2 kpc from the galaxy center. The decrease in polarized flux toward the nucleus (Fig. 2) support a slow dimming of the source, where the time delay expected between direct and scattered light produces an echo of past nuclear activity (Hutsemékers et al. 2019), either by a faded AGN or by a past elevated rate of TDEs. Non-null polarization degrees (p) in annuli centered on the nucleus indicate that the polarization is not perfectly centrosymmetric, i.e., the scattering regions are not isotropically distributed and/or homogeneous, consistent with the non-axisymmetric morphology of the EELR revealed by the MUSE data of GSN 069 (Wevers et al. 2024). The polarization angle (θ) measured in annuli at ~4–5″(~1.5–2 kpc) from the nucleus (Fig. 2) and within a circular aperture of ~6.3″(~2 kpc) (Table 1) reveal a dominant polarization direction of ~140°. Assuming this scattering lead by the EELR, then the EELR axis should be perpendicular to $\theta \sim 140°$, where θ is measured with respect to the north–south (N-S) direction (the IPOL adapter position). To further investigate the EELR morphology, we computed Hα, [OIII]$\lambda5007$, and [NII]$\lambda6583$ line maps from archival GSN 069 MUSE observations (see Appendix B). As shown in Fig. B.2, the EELR axis, as inferred from θ, aligns with elongated gas distributions seen in the NE area of the three emission-line maps. This suggests a preferred direction in the illuminating photon field. This geometry is more naturally explained by fossil polarization–ionization cones shaped by a faded AGN and its long-lived torus structure, rather than by past episodes of enhanced TDE activity, which are not expected to maintain any sustained collimating structure (an arbitrary aperture for the polarizaton–ionization cones of 60°is drawn in Fig. B.2 to guide the eye). This torus-shaped, biconical pattern favor the faded AGN as the origin for the EELR. However, because this geometry remains tentative, our results cannot rule out the past elevated TDE rate scenario.

The spectropolarimetry in the southern regions gives $\theta \sim 100°$ (Fig. 4), i.e., roughly perpendicular to the hypothetical line connecting the nucleus with the scattering regions within our slit. Since scattering generates a polarization angle perpendicular to the photon's last direction of flight before being scattered, the source that illuminated the southern scattering regions in the past should be the nucleus itself. The 10° departure to 90° in the south extractions together with a higher θ in the northern region can be explained again by the non-axisymmetric EELR reported by Wevers et al. (2024).

4. Conclusions

1. The nucleus of GSN 069 is compatible with null intrinsic polarization, but the polarization degree increases as we move away from the galaxy center (Fig. 2 and 4), indicating polarization by scattering. In the southern regions, the polarization angle suggests illumination by the switched-off nucleus, i.e., a polarization echo from past nuclear activity. In the northern region, the different polarization angle reveals nonhomogeneous or non-isotropic scattering regions. These results are consistent with the detection of an EELR of non-axisymmetric morphology revealed by the MUSE data Wevers et al. (2024).

2. The proved intrinsic and radial increasing polarization demonstrates a switched-off nucleus compatible with both a faded AGN and a past elevated TDE rate. The polarization angle defines an axis that aligns with the gas distributions, revealing an EELR consistent with tentative relic polarization cones. This would suggest the presence of a torus in the past. Therefore, the polarimetry supports geometrically the faded AGN scenario, although TDEs cannot be ruled out.

3. Broad-emission lines (BELs) are not detected in polarized light. Instead, narrow-emission lines (NELs) are seen in the polarized flux, more intense in the southern regions.

4. We found a bright spot at ~4.25″ south of the nucleus. As all the analyzed direct spectra (see Fig. 1), it is classified as an AGN according to BPT diagrams (Fig. A.1) and lacks continuum emission and BELs.

References

Arcodia, R., Merloni, A., Nandra, K., et al. 2021, Nature, 592, 704
Arcodia, R., Liu, Z., Merloni, A., et al. 2024, A&A, 684, A64
Arcodia, R., Baldini, P., Merloni, A., et al. 2025, ApJ, 989, 13
Bagnulo, S., Landolfi, M., Landstreet, J. D., et al. 2009, PASP, 121, 993
Bykov, S. D., Gilfanov, M. R., Sunyaev, R. A., & Medvedev, P. S. 2025, MNRAS, 540, 30
Cappellari, M. 2017, MNRAS, 466, 798
Cardelli, J. A., Clayton, G. C., & Mathis, J. S. 1989, ApJ, 345, 245
Cazzoli, S., Márquez, I., Masegosa, J., et al. 2018, MNRAS, 480, 1106
Chakraborty, J., Kara, E., Masterson, M., et al. 2021, ApJ, 921, L40
Chakraborty, J., Kara, E., Arcodia, R., et al. 2025, ApJ, 983, L39
Cikota, A., Patat, F., Cikota, S., & Faran, T. 2017, MNRAS, 464, 4146
de Vaucouleurs, G. 1948, Ann. Astrophys., 11, 247
French, K. D., Earl, N., Novack, A. B., et al. 2023, ApJ, 950, 153
Gaskell, C. M. 1982, ApJ, 263, 79
Giustini, M., Miniutti, G., & Saxton, R. D. 2020, A&A, 636, L2
González-Gaitán, S., Mourão, A. M., Patat, F., et al. 2020, A&A, 634, A70
Goodwin, A. J., Arcodia, R., Miniutti, G., Miller-Jones, J. C. A., & van Velzen, S. 2025, PASA, 42
Guolo, M., Mummery, A., Wevers, T., et al. 2025, ApJ, 985, 146
Hernández-García, L., Chakraborty, J., Sánchez-Sáez, P., et al. 2025, Nat. Astron., 9, 895
Hutsemékers, D., Agís González, B., Marin, F., et al. 2019, A&A, 625, A54
Kewley, L. J., Dopita, M. A., Sutherland, R. S., Heisler, C. A., & Trevena, J. 2001, ApJ, 556, 121
Linial, I., & Metzger, B. D. 2023, ApJ, 957, 34
Linial, I., Metzger, B. D., & Quataert, E. 2025, ApJ, 991, 147
Marin, F. 2018, A&A, 615, A171
Marin, F., Hutsemékers, D., Jiang, C. Z., et al. 2025, A&A, 695, A55
Miller, J. S., & Antonucci, R. R. J. 1983, ApJ, 271, L7
Miniutti, G., Saxton, R. D., Rodríguez-Pascual, P. M., et al. 2013, MNRAS, 433, 1764
Miniutti, G., Saxton, R. D., Giustini, M., et al. 2019, Nature, 573, 381
Miniutti, G., Giustini, M., Arcodia, R., et al. 2023, A&A, 670, A93
Moehler, S., Modigliani, A., Freudling, W., et al. 2014, A&A, 568, A9
Mummery, A., Guolo, M., Matthews, J., et al. 2025, MNRAS, 544, 2262
Nicholl, M., Pasham, D. R., Mummery, A., et al. 2024, Nature, 634, 804
Patat, F., & Romaniello, M. 2006, PASP, 118, 146
Plaszczynski, S., Montier, L., Levrier, F., & Tristram, M. 2014, MNRAS, 439, 4048
Quintin, E., Webb, N. A., Guillot, S., et al. 2023, A&A, 675, A152
Schlafly, E. F., & Finkbeiner, D. P. 2011, ApJ, 737, 103
Serkowski, K., Mathewson, D. S., & Ford, V. L. 1975, ApJ, 196, 261
Sérsic, J. L. 1968, Atlas de Galaxias Australes
Sluse, D., Hutsemékers, D., Lamy, H., Cabanac, R., & Quintana, H. 2005, A&A, 433, 757
Tran, H. D. 1995, ApJ, 440, 578
Valdes, F., Gupta, R., Rose, J. A., Singh, H. P., & Bell, D. J. 2004, ApJS, 152, 251
van Dokkum, P. G., Bloom, J., & Tewes, M. 2012, Astrophysics Source Code Library [record ascl:1207.005]
Wevers, T., & French, K. D. 2024, ApJ, 969, L17
Wevers, T., Pasham, D. R., Jalan, P., Rakshit, S., & Arcodia, R. 2022, A&A, 659, L2
Wevers, T., French, K. D., Zabludoff, A. I., et al. 2024, ApJ, 970, L23

Appendix A: Observations and data reduction

The observations of GSN 069 were carried out on 6 September 2019 in visitor mode (Program ID: 0103.B-0791) using the European Southern Observatory (ESO) Very Large Telescope (VLT) equipped with the FOcal Reducer and low dispersion Spectrograph 2 (FORS2) mounted at the Cassegrain focus of Unit Telescope #1 (Antu). Linear polarimetry was performed with the standard setup and using the stripped mask. GSN 069 was positioned at the center of the field of view to avoid the significant off-axis instrumental polarization generated by the FORS2 optics (Patat & Romaniello 2006; González-Gaitán et al. 2020). All observations were carried out at an airmass ≲ 1.5. After bias subtraction and flat-field correction, every frame was processed to remove cosmic rays using the lacosmic Python package (van Dokkum et al. 2012).

A.1. IPOL mode: Imaging polarimetry

Polarized images were secured with the filter V_HIGH+114 (λ_c = 5550 Å; FWHM= 1232 Å), using the standard resolution collimator and 2×2 binning, which corresponds to a scale plate of 0.25" pixel^{-1} and to a field of view (FoV) of $6.8' \times 6.8'$ imaged onto two identical CCD detectors (CHIP1 and CHIP2). A sequence of four exposures of 30 s each (4×30 s) was performed for GSN069 with the HWP rotated at 0°, 22.5°, 45°, and 67.5° angles. In order to measure the polarization of bright field stars around GSN 069 we switched to a 1×1 binning and 4×3 s exposures. The seeing remained stable and around 0.7" during the imaging polarimetry observations.

Data reduction of our imaging polarimetry data was performed using the procedures described in Sluse et al. (2005). Polarized (BD-12 5133 and Vela1 95) and unpolarized (WD 1620-391) standard stars (Cikota et al. 2017) were observed and reduced in the same way to check the whole reduction process. We measured a polarization degree for the unpolarized standard star of $0.06 \pm 0.06\%$, indicating that the residual instrumental polarization is negligible at the center of the field.

GSN 069 is situated at high galactic latitude ($b = -80.8°$), well away from the galactic plane. Thus, the expected spurious polarization induced by the interstellar medium (ISM) of our Galaxy should be negligible. Actually, following the galactic dust reddening and extinction tool provided by IRSA [1] and Serkowski et al. (1975), we found that $p_{ISM\ max} \lesssim 0.24\%$.

We have also estimated the polarization of the stars lying on the FoV of FORS2, assuming that p_{ISM} should be constant along the $6.8' \times 6.8'$ area covered by the instrument. There exists a radial instrumental polarization pattern across the CCD increasing to $\approx 1.4\%$ at the edges, depending on the filter, caused by the optics of the dual-beam polarimeter of FORS2, and very well characterized (Patat & Romaniello 2006; González-Gaitán et al. 2020). Unfortunately, it was only possible to measure the polarization of a single field star. For that star, we found $p = 0.38 \pm 0.06\%$ and $\theta = 102° \pm 4°$, which become $p = 0.32 \pm 0.06\%$ and $\theta = 105° \pm 4°$ after applying the instrumental correction maps developed by González-Gaitán et al. (2020), in reasonable agreement with the upper limit $p_{ISM\ max} \lesssim 0.24\%$. In conclusion, p_{ISM} cannot be inferred, only upper limits. Therefore and hereafter (also in spectropolarimetry), we do not apply any correction to compensate for the galactic interstellar contamination.

The polarization of GSN 069 was measured in various apertures to estimate the impact of the host galaxy. Figures 1 and B.2

---

[1] https://irsa.ipac.caltech.edu/applications/DUST/

show the different regions/subslits defined along the manuscript. Table 1 gives the polarization quantities measured within the apertures drawn in Fig. 1. The polarization degree has been debiased following the prescriptions of Plaszczynski et al. (2014) and it is indicated as p_0 in Table 1 .

Finally, we tried to build polarization maps from the IPOL images, but the polarization signal along with the spatial resolution are not sufficient to compute reliable maps, which would require subpixel precision.

A.2. PMOS mode: Spectropolarimetry

Polarized spectra were secured with the grism 600B+22 (λ_c = 4627Å; λ_{range} = 3300 − 6210Å) using a slit width of 1", which provides a dispersion of 0.75 Å pixel^{-1} and a spectral resolution of $R = \lambda/\Delta\lambda = 780$. To obtain simultaneous observations of Hβ and Hα, we shifted the position of the slit on the EV2 detector to cover the spectral range $\sim 3800 - 6700$Å. The binning was 2×2 and the scale plate 0.25"/pixel. The seeing oscillated between 0.59" and 1.34" during spectropolarimetry, i.e., reaching values comparable to and higher than the slit width.

A sequence of four exposures of 1800 s each, with the HWP rotated at 0°, 22.5°, 45°, and 67.5° angles, constituted one observing block (OB). It was repeated three times, i.e., three OBs of about 2h15min each, so that the better signal-to-noise (S/N) could be achieved by (median) combining the different spectra and checking the consistency among the three sets. The instrument position angle was set to $PA = 0°$ (that is, along the N-S direction).

In total, we obtained 24 spectra (from two orthogonal polarizations, four HWP angles, three OBs). The normalized Stokes parameters $q(\lambda)$ and $u(\lambda)$, corrected for the HWP chromaticity, as well as the linear polarization degree $p(\lambda)$ and the polarization position angle $\theta(\lambda)$ were computed from the individual, sky-subtracted, spectra following standard formulae (e.g., Bagnulo et al. 2009; Marin et al. 2025).

The polarized standard star BD-12 5133 (Cikota et al. 2017) was observed and reduced in the same way to check the whole reduction process in spectropolarimetry. The spectrophotometric standard star Feige 110 (Moehler et al. 2014) was observed, also in spectropolarimetric mode, to generate a response curve and flux-calibrate the direct spectrum of GSN 069.

Due to the good S/N, we extracted a central narrow region within a subslit of 5-pixel width (Fig. 1), corresponding to 1.25" or $\sim 1\sigma$, being σ the average seeing value during spectropolarimetry. This represents the nucleus of GSN 069 with a minimal contribution of the host galaxy, having checked that wider/narrower regions/subslits do not provide any extra information.

Even if the S/N in terms of direct flux is high, when the polarized signal is low, its corresponding probability distribution differs from Gaussian. To avoid the positive bias associated with the polarization degree p, a common practice is to rotate the plane $q - u$ by an angle θ, being θ the inferred polarization angle, so that all the signal is contained in q' and Gaussian errors can be considered. For our data, this rotation does not provide us with an improved view of our results, and we decided to show the standard polarization degree p and position polarization angle θ.

A.3. PMOS mode: Direct spectrum

We computed the direct spectrum of GSN 069 by adding up the 24 individual spectra taken in PMOS mode. After flux-
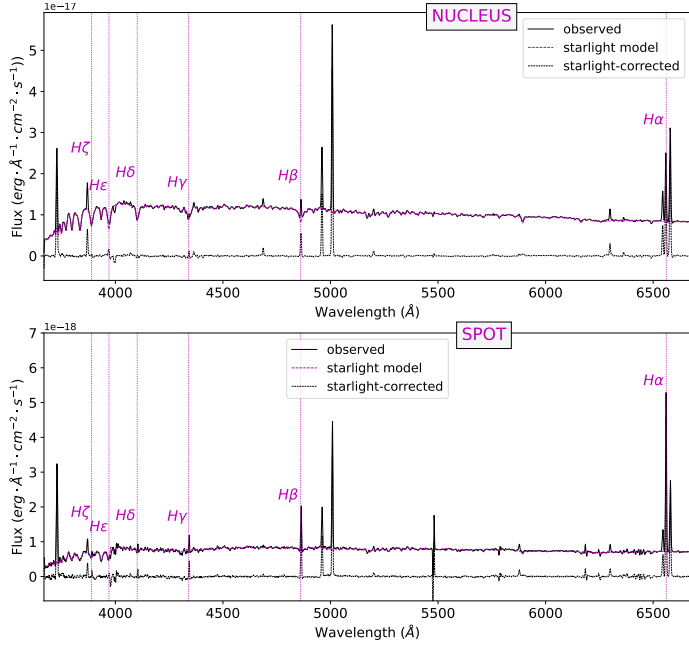
Fig. A.1. Direct spectra of the nucleus of GSN 069 (1.25″extraction, upper panel) and the southern spot (2.25″extraction, lower panel). The starlight model (magenta) has been subtracted from the observed spectrum (black) to generate the emission-line spectrum (dashed line).
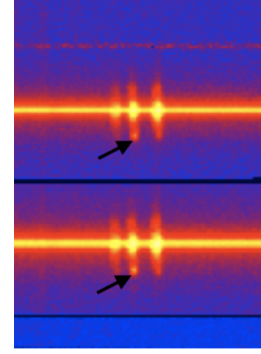

Fig. B.1. Bright feature located 4.25″ south of the nucleus, which we refer to as the southern spot, as seen in the spectral images by zooming on the Hα + [NII] spectral region. Ordinary (upper) and extraordinary (lower) spectra at one position of the HWP. The height of each strip is about 20".

[O I]λ6300/Hα are for the nucleus (southern spot), in logarithm: 0.94 ± 0.01 (0.52 ± 0.01), 0.145 ± 0.005 (-0.27 ± 0.01) and -0.77 ± 0.02 (-1.20 ± 0.06), which places both regions in the AGN section of the diagnostic diagrams. The direct spectra corresponding to the north and south extractions of the host galaxy are shown in Fig. C.1. BPT narrow-line ratios also indicate an AGN classification for both regions (Appendix C).

calibrating the spectrum, by using the response curve generated with the spectropolarimetric observations of the spectrophotometric standard star Feige 110, we corrected for the galactic absorption along the line of sight throughout Cardelli's extinction law (Cardelli et al. 1989), considering $E(B-V) = 0.0232 \pm 0.0009$, as reported by Schlafly & Finkbeiner (2011) and using the python package `dust_extinction` v1.2.[2] Since the seeing value exceeded temporarily the slit width, we may expect a wavelength-dependent slit loss. Assuming a point-like source observed through a 1" slit with a seeing of 1.3", the considered line flux ratios will not be affected by more than 3%, and slit loss can be neglected.

We estimated the host galaxy contribution to the observed spectra by modeling the stellar continuum and absorption features (e.g., MgI $\lambda\lambda$5167,5173,5184) following the same procedure as Cazzoli et al. (2018). Briefly, we used the penalized PiXel-Fitting code (pPXF) by Cappellari (2017) and references therein, with the Indo-U.S. stellar library (Valdes et al. 2004). In this library, there are 885 stars, with a continuous spectral coverage from 3460 to 9464 Å, selected to provide us with a broad coverage of the stellar atmospheric parameters (effective temperature, surface gravity, and metallicity). We modeled the stellar component for the entire wavelength range of our spectra to avoid introducing inconsistencies or biases that affect the emission line ratios, so that the best-fit stellar spectrum can be subtracted from the observed one to obtain a pure spectrum for the nuclear emission. The nuclear spectrum (Fig. A.1) shows Balmer lines in absorption from Hβ onward. After starlight correction, Hγ and Hϵ clearly arise in emission along with a weak Hδ. We have performed line fitting around Hα and Hβ on the starlight-corrected spectra (Fig. D.1). From the same line-fitting (see appendix D for details), we have derived the standard emission line ratios used in the BPT diagrams (Kewley et al. (2001) and references therein). [O III]λ5007/Hβ, [N II]λ6583/Hα, and

Appendix B: Southern spot and MUSE data

In every spectral image, we detected a bright feature located 4.25″ south of the nucleus, which we refer to as the southern spot, visible in both orthogonal polarizations and most prominent in the Hα emission (Fig. B.1). We extracted the direct spectrum and the normalized Stokes parameters of the spot following the same procedure as for the nucleus, but using a 9-pixel (2.25″) subslit centered on the spot (Fig. 1). The broader extraction, compared to that of the other regions, was adopted to encompass the entire feature along the spatial direction.

The spot is not seen in our optical images, but in Chandra data (Miniutti et al. 2019). To further investigate its presence, we inspected the ESO archive and found the run/programme ID 109.238W.007/0109.B-0871(G) "A filler program for the apocalypse: end all weather-idle-time on UT4 in P109", PI: Bian. This program includes MUSE data of GSN 069 taken in July 2022, 27th with a total exposure time of 3000 s and an effective spatial resolution of 1.22". Because the southern spot appears brigher in Hα in our FORS2 spectra, we isolated that line in the MUSE data using `QFitsView 4.1`.[3] The resulting Hα emission map shown in Fig. B.2 clearly reveals the spot. Trying to resolve the EELR structure, we also isolated the [OIII]λ5007 and [NII]λ6583 line maps (Fig. B.2). In the three cases, the axis perpendicular to the polarization angle θ, aligns with elongated gas distributions at the NE. This also traces a preferred direction in the illuminating photon field, favoring a geometry more consistent with a long-lived torus structure of a faded AGN than with a morphology shaped by a past intense TDE activity that is not expected to sustain nor maintain collimating structures.
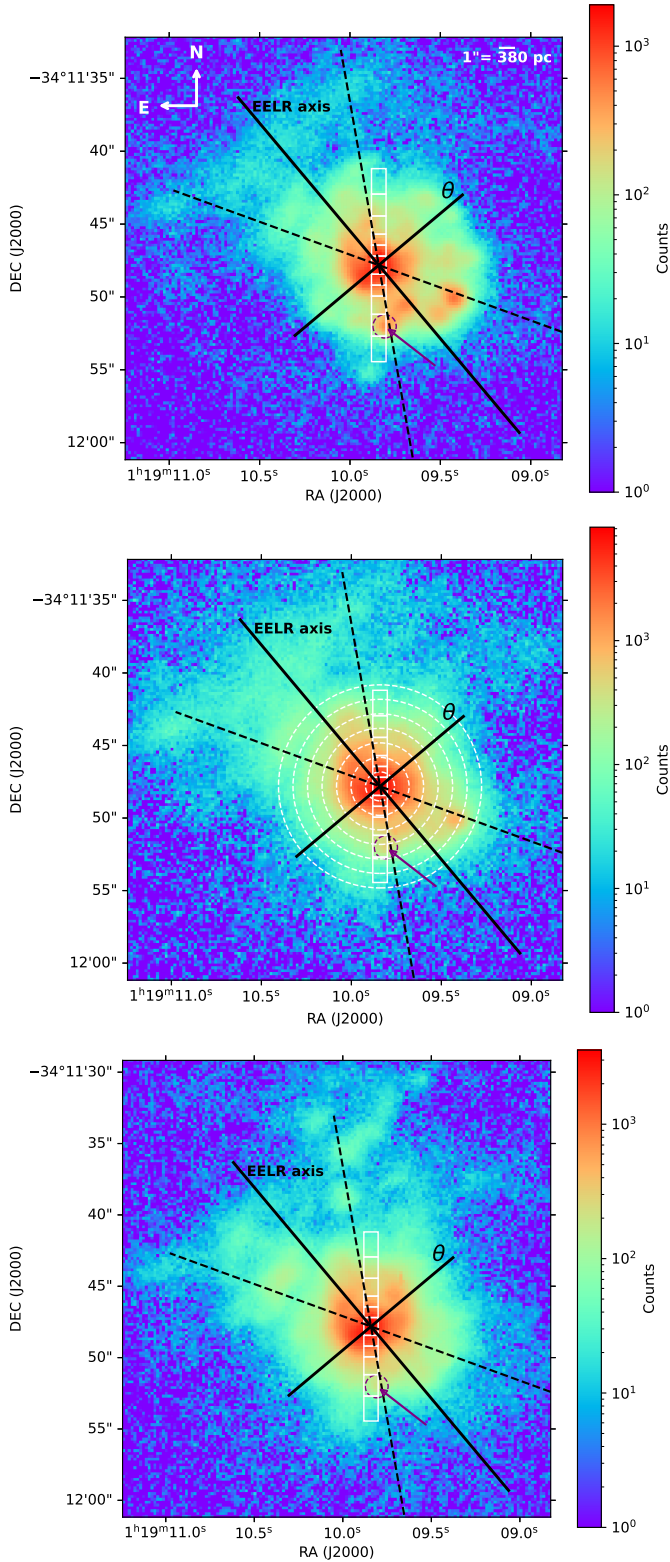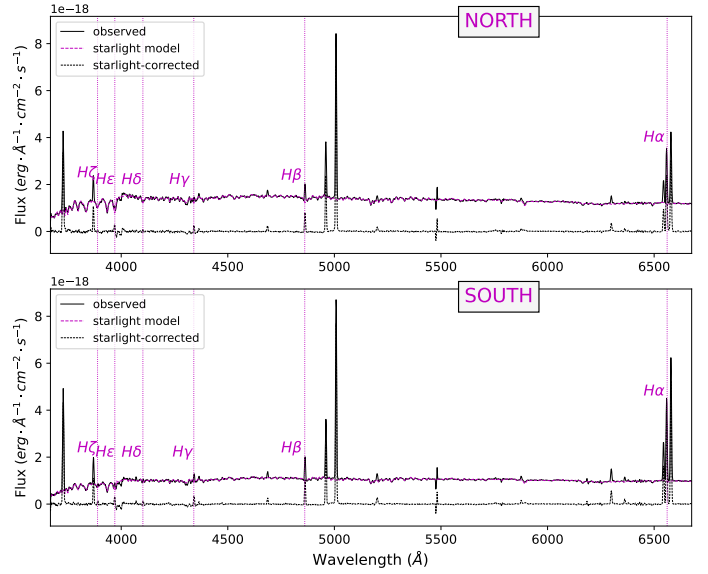

Fig. C.1. Direct spectra of the regions north and south of the nucleus of GSN 069 (both 1.25″ extractions). The starlight model is represented in magenta. The starlight model has been subtracted from the observed spectrum to generate the starlight-corrected spectrum shown at the bottom of each panel with a dashed line.

Appendix C: Host extractions north and south of the nucleus

The direct and polarized spectra of the host galaxy were also extracted using 5-pixel (1.25″) subslits located north and south of the nucleus (Fig. 1). Figure C.1 shows the direct spectra for the north and south regions, with starlight subtraction done as explained in Sect. A.1. The line ratios in the north (south) region are, in logarithm: [OIII]λ5007/H$_\alpha$ = 0.95 ± 0.02 (0.85 ± 0.02), [N II]λ6583/H$_\alpha$ = 0.11 ± 0.01 (0.157 ± 0.005), and [O I]λ6300/H$_\alpha$ = 0.85 ± 0.03 (−0.80 ± 0.03), which in the BPT diagrams translates into AGN classifications for both regions.

Figure C.2 shows the polarized spectra for the north and south regions.

Appendix D: Broad line fitting

Figure D.1 shows the line fitting around Hα and Hβ for the direct spectra of nucleus of GSN069 and the southern spot. Narrow lines were modeled as single Gaussians (Lorentzians provided worst residuals). Spectral lines belonging to the same doublet were assumed to have the same FWHM. A second broad Gaussian was added to check if the statistic improves, using `curve_fit`, but that is not the case, while the results are not physically meaningful. As common in optical emission-line fitting, underestimated pixel uncertainties give meaningless reduced χ^2, in this case with and without broad Gaussian $\sim$ 13. The covariance matrix has been re-scaled by the reduced χ^2 factor to obtain realistic parameter uncertainties.

Since the south extractions are the ones with higher polarization, we also carried out line fitting on the corresponding polarized spectra, even if those are noisy, to rule out the presence broad Balmer components there. With the polarized spectra, if broad Gaussians were tied to the narrow component, the fitting did not converge. Nonetheless, offsets between BELs and NELs are seen in AGNs (Gaskell 1982). In the south extraction, the reduced χ^2 does not improve by adding broad Gaussians, which

Fig. B.2. *Upper panel:* MUSE continuum-subtracted Hα image. *Middle panel:* MUSE continuum-subtracted [OIII]λ5007. *Lower panel:* MUSE continuum-subtracted [NII]λ6583. The position of the southern spot is marked with a purple arrow and circle. The white solid boxes denote the spectropolarimetry bins corresponding to Fig. 2, while the dashed white circles account for the annular regions of Fig. 4 (only shown in the middle panel for clarity). The direction corresponding to the polarization angle θ and its perpendicular are superimposed. The latter direction represents the proposed EELR axis. The black dashed lines represent an arbitrary 60° aperture for the ionization cones, drawn to guide the eye.
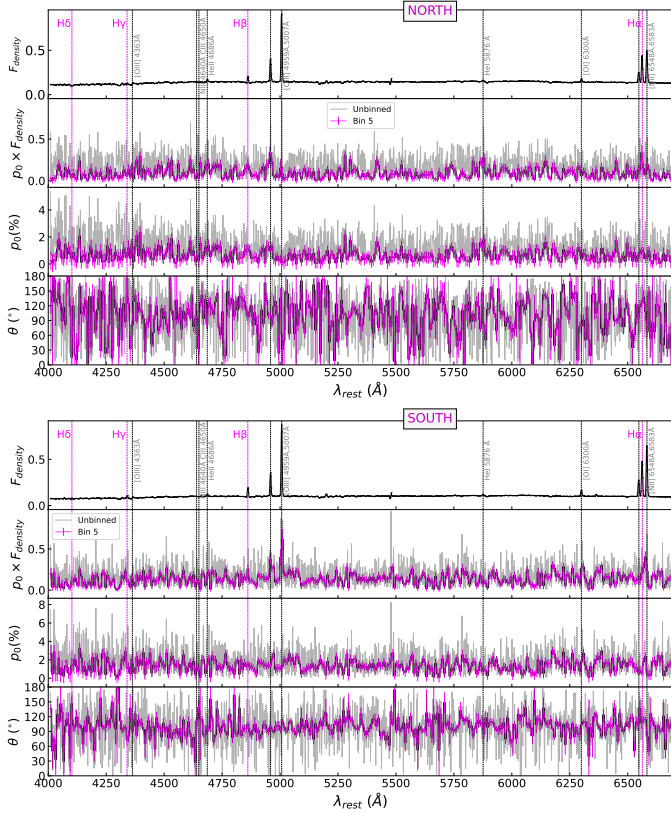
Fig. C.2. Flux density in arbitrary units ($F_{density}$), polarized flux ($F_{density} \times p_0$), debiased polarization degree (p_0), and polarization angle (θ) for the north (upper panel) and south (lower panel) regions.
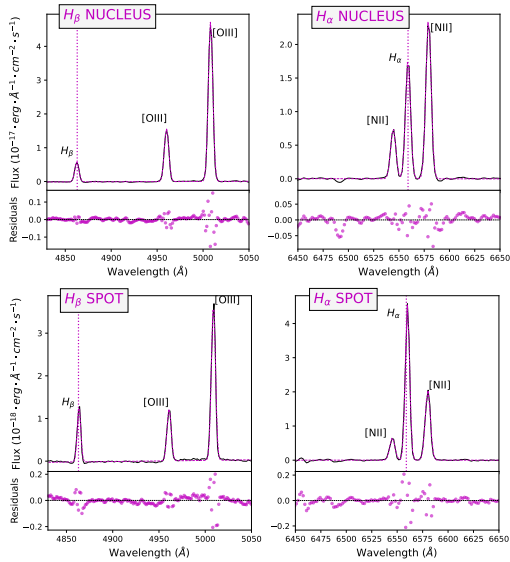

Fig. D.1. Line fitting and corresponding residuals in the Hβ and Hα wavelength ranges for the direct nucleus spectrum of GSN 069 (upper panel) and the southern spot (lower panel).

Fig. D.2. Line fitting and corresponding residuals for the polarized spectrum of the south (upper row) and the southern spot (lower row) extractions in the Hβ and Hα wavelength ranges. As shown in the inset, the addition of broad emission line components is never significant.

are neither physically meaningful (see figure D.2 for the statistics). Applying the same fitting for the southern spot (figure D.2) the broad components are neither statistically required nor physically justified.